MSc in Photonics

PHOTONICS**BCN**

Universitat Politècnica de Catalunya (UPC)
Universitat Autònoma de Barcelona (UAB)
Universitat de Barcelona (UB)
Institut de Ciències Fotòniques (ICFO)

http://www.photonicsbcn.eu

Master in Photonics

MASTER THESIS WORK

Nano-structured surfaces for mid-infrared optical sensing

Javier Arrés Chillón

Supervised by Dr. Valerio Pruneri, (ICFO)

and co-supervised by Dr. Bruno Paulillo, (ICFO)

Presented on date 9th September 2019

Registered at

Escola Tècnica Superior d'Enginyeria de Telecomunicació de Barcelona

Nano-structured surfaces for mid-infrared optical sensing

Javier Arrés Chillón

ICFO-Institut de Ciencies Fotoniques, The Barcelona Institute of Science and Technology, Mediterranean Technology Park, Castelldefels (Barcelona), Catalonia, Spain

E-mail: javierarreschillon@gmail.com

Abstract. We design and realize two nano-structured surfaces that support graphene plasmon modes for sensing applications in the mid-infrared range. More specifically the two designs are engineered on a CaF_2, IR-transparent, substrate which allow backlight illumination, which is suitable for biosensing in aqueous medium. The nano-structured surfaces have the objective to combine thin metal structures with a graphene layer to engineer graphene plasmon modes generation at wavelengths difficult to obtain in single graphene structures. The designs are first modeled with Finite Element Method Analisys (FEM), using COMSOL, and then fabricated and tested.

1. Introduction

Optical biosensing techniques based on enhanced light-matter interaction allow label free and non-destructive detection of molecules [1, 2]. Visible $(0.38-0.78)\mu m$ and near-infrared (near-IR) $(0.78-3)\mu m$ light is used for refractometric sensing, where spectral shift of surface plasmons (SPs) modes are detected due to changes of refraction index. On the other hand, mid-infrared (mid-IR) $(3-12)\mu m$ radiation is used for infrared absorption spectroscopy techniques that target the vibrational modes of the molecules [3]. However the molecular absorption cross-sections in the mid-IR are low due the mismatch between molecular dimensions (nanometers) and light wavelength requiring large quantity of analytes.

This issue can be overcome using plasmonic modes to create free-label, non-destructive and high-sensitive sensing platforms of molecules with IR light. In particular, localized surface plasmon resonances (LSPRs) in nano-structured metal-dielectric surfaces,[4] can be engineered to generate and confine electric fields in subwavelength regions with enhancements factors of $(10-10^4)$ times the incident electric field.

Surface-enhanced Raman scattering (SERS) [1] or surface-enhanced infrared absorption (SEIRA) [2] are the two major LSPRs based techniques for biosensing, each one working in visible/near-IR and mid-IR spectra, respectively. For instance, SEIRA uses LSPRs to increase the light-matter interaction between plasmonic nano-antennas

and molecular vibrational modes, so it can be used as a sensitive molecular fingerprint spectroscopy technique.

SEIRA based on localized graphene plasmons (GPs) generation in nano-structured graphene has been used to obtain spectral tuneability and large field confinement [5, 6, 7].

In this thesis, two novel nano-structured surfaces based on GPs generation are design for reliable *in-situ* biosensing that can work either with dried samples or with samples in aqueous media. The plasmonic surfaces will be engineered in CaF_2 substrate in order to allow backlight incidence, see fig. 1.

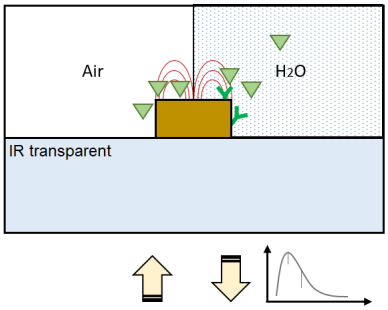

Figure 1: Schematic representation for *in-situ* biosensing with dried analyte samples (air media) and with suspended samples (aqueous media) in backlight incidence.

2. State of the art

In order to generate SPs, tailored nano-structures of noble-metals such as nano-antennas have been used for sensing, however, they lack of spectral tuneability and shows relatively small confinement of the fields generated [8, 9, 10, 11].

On the other hand, graphene nanoribbons over SiO2/Si substrate have been used to excite localized GPs modes with tuneable the Fermi Energy to detect amide I & II protein bands [5]. However, typical extinction values obtained are $\approx$ 10% in transmission reading and even weaker in reflection. To enhance the signal in reflection with top incidence, Salisbury screens are typically used in combination with graphene and quasi perfect absorption can be obtained [12]. For those systems, the light incidence and spectral reading cannot be done with backlight incidence, due the high substrate reflection, so they are not applicable for realistic *in-situ* biosensing and are restricted to the sensing of dried molecules.

Recently, acoustic graphene plasmons (AGPs), [13, 14], generated from hybridization between GPs carrier oscillations and mirror, out-of-phase oscillations of a metal near the graphene layer, have been used for the detection of amide I & II bands. AGPs structures shows largest field confinement in the graphene-metal gap, which is difficult to use *in situ* biosensing. However large field confinement can be obtained in the graphene layer vicinity if the geometry of the structure is properly designed.

Lastly, a combination of continuous graphene sheets and metal nano-antennas have also been used for sensing applications. These hybrid structures can be used as a source

for tuneable SPs in the nano-antennas due the electrical tuneability of graphene [15]. Also, it has been theoretically predicted that these structures can generate GPs modes in the free metal regions, simulating similar behaviour than patterned graphene [16, 17].

3. Optical properties of Graphene. Graphene plasmons

The optical properties of graphene can be described by its optical conductivity, which in the mid-IR spectra is described by the Kubo's formula [18]:

$$\sigma_{intra} = \frac{\sigma_0}{\pi}\frac{4}{\hbar(\gamma_G - iw)}\left[E_F + 2k_BT\ln\left(1 + e^{(-E_F/k_BT)}\right)\right] \quad (1)$$

where $\sigma_0 = e^2/4\hbar$ is the intrinsic optical conductivity of graphene, w is the angular frequency of light, $\gamma_G = 1/\tau_G$ is the decay rate of the graphene electrons and E_F is the Fermi energy level of graphene. T is the temperature and $\hbar$ and k_B the Planck and Boltzmann constants, respectively. The decay rate of the graphene's electrons is related with the carrier mobility that in unpatterned graphene sheets reach values of $10^{3-4}cm^2/Vs$ [18]. The Fermi energy of graphene is proportional to the density of carriers, which can be changed by doping o by an external electrical tuning. The relative permitivity of graphene is related with the optical conductivity with:

$$\varepsilon_r(w) = 1 + \frac{i\sigma(w)}{\varepsilon_0 w\delta_G} \quad (2)$$

being $\delta_G = 0.3nm$ the graphene layer thickness and ε_0 the vacuum permitivity.

Despite the remarkably high absorption of graphene being a 2D material, the coupling between plasmonic excitations in single graphene sheets and electromagnetic radiation is not efficient enough for sensing applications. In order to overcome this limitation, engineered graphene structures with sizes smaller than the incident wavelengths can be used to generate GPs modes [19]. Either in homogeneous graphene sheets or in graphene structures, the plasmon dispersion for the GPs is given by [20]:

$$q(w) = \frac{\pi\hbar^2\varepsilon_0(\varepsilon_{r1} + \varepsilon_{r2})}{e^2E_F^*}\left(1 + \frac{i}{\tau_G w}\right)w^2 \quad (3)$$

where for simplification $E_F^* = E_F + 2k_BT\ln\left(1 + e^{(-E_F/k_BT)}\right)$. In eq.(3), ε_{ri} represents the relative permitivity of the upper ($i = 1$) and bottom ($i = 2$) media. In the case of structured graphene, the momentum dispersion of the GPs are restricted to the eigenmodes of the engineered structure [21].

Here, Finite Element Method Analisys (FEM) with COMSOL is used to optimize the value of the geometrical parameters of the novel nano-structures to obtain plasmonic modes of graphene near $\lambda \approx 7\mu m$. Graphene is modeled as a $2D$ material with thickness $\delta_G = 0.3nm$ and his permitivitty given by eq.(2). The plasmon lifetime goes from $\tau_G = 100fs$ to model high-Q graphene to $\tau_G = (20 - 30)fs$ for nanopatterned and the Fermi energy can sweep between $E_F = (0.1 - 0.4)eV$ with gating. The optical dispersion models of the materials that will be used: Au, SiO_2 and CaF_2 are obtained

from [22, 23, 24], respectively. For gold thin layers, the damping rate in the Lorentz model [22] is phenomenologically multiplied by a factor 3, to account for the change in optical properties as compared to thick films as described in [8].

4. Novel graphene based plasmonic nano-structures

The first design is a modification of the AGPs surface structure described in [14]. The system consists of a series of Au/SiO_2 nanoribbons engineered on a CaF_2 substrate with a graphene layer covering the ribbon structure, fig. 2a, 2b. The thickness of the gold and SiO_2 ribbons are $t_{Au} = 3nm$ and $t_{SiO_2} = 10nm$, respectively. The width and periodicity are w and $\Lambda = w + s$, respectively, being s the separation between the ribbons. Due to the ribbon like geometry, the dispersion of the AGPs modes must follow $q \propto (w + s)^{-1}$ [14, 19, 21].

In figure 3a the resonance peak curves for the plasmonic dispersion are plotted for different values of w and s, in backlight and normal angle incidence and with the electric field polarised across the ribbons. It can be seen that when the width of the Au/SiO_2 nanoribbons increase, the plasmonic modes shift towards larger wavelengths and for larger enough nanoribbons widths higher plasmonic modes appears. Also, the resonance peak values maximizes for an specific ribbon width and separation values. Moreover, when the separation between the nanoribbons increase, the resonance peaks shift towards larger wavelengths and decreases the overall peak values. Is important to take into account the effect of SiO_2, because when the plasmonic resonances falls near his phonon band, approaching the prohibited Reststrhalend band, the resonances peaks collaps and decrease [4]. For comparison, GPs modes are also plotted for graphene nanoribbons with the same widths and separations combinations in CaF_2, fig. 3a. They show higher peak values for the first GPs mode but for widths that are difficult to engineer. Then, although the resonance peaks are slightly lower for the novel AGPs nano-structure than for the graphene nanoribbon, the design proposed is advantageous since it allows to excite plasmons at same wavelength with structured dimensions easier to fabricate.

Figure 3b shows the absorption contribution at different regions for $w = 70nm$ and $s = 20nm$, proving that most part of the energy is stored in the graphene layer. The inset shows the field distribution in the unit cell for the first mode, showing the AGPs in the SiO_2 and the decay of the field in the graphene vicinity.

In figure 3c, the plasmon decay is plotted at two different lines of the unit cell, see inset. The plasmon decay is obtained as the absolute value of the y-component of the electric field, $|E_y|$. The plot proves that although the field is more enhanced in the graphene-metal gap, the field decay in the upper part of the nano-structure can be exploited for biosensing applications.

Lastly, the plasmon dispersion is plotted for different Fermi energies, fig. 3d, showing the displacement of the absorption peaks which prove the generation of graphene plasmons.

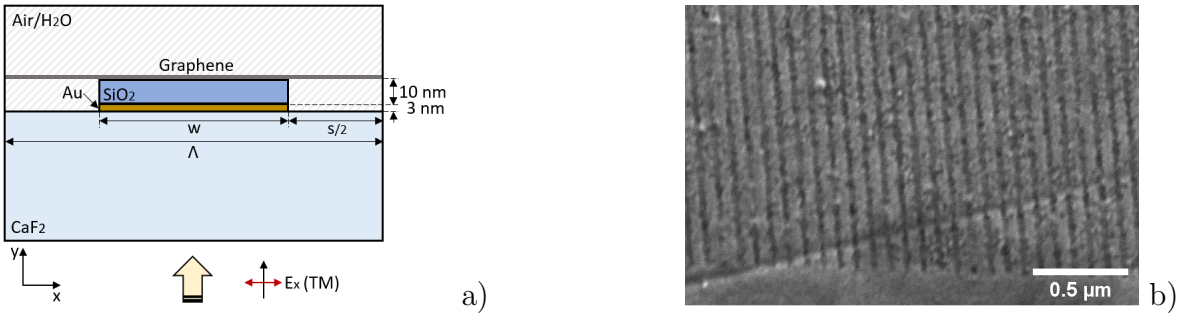

Figure 2: **a)** Schematic representation of the hybrid Au/SiO_2 ribbon-Graphene sensor. **b)** SEM image of the sensor.

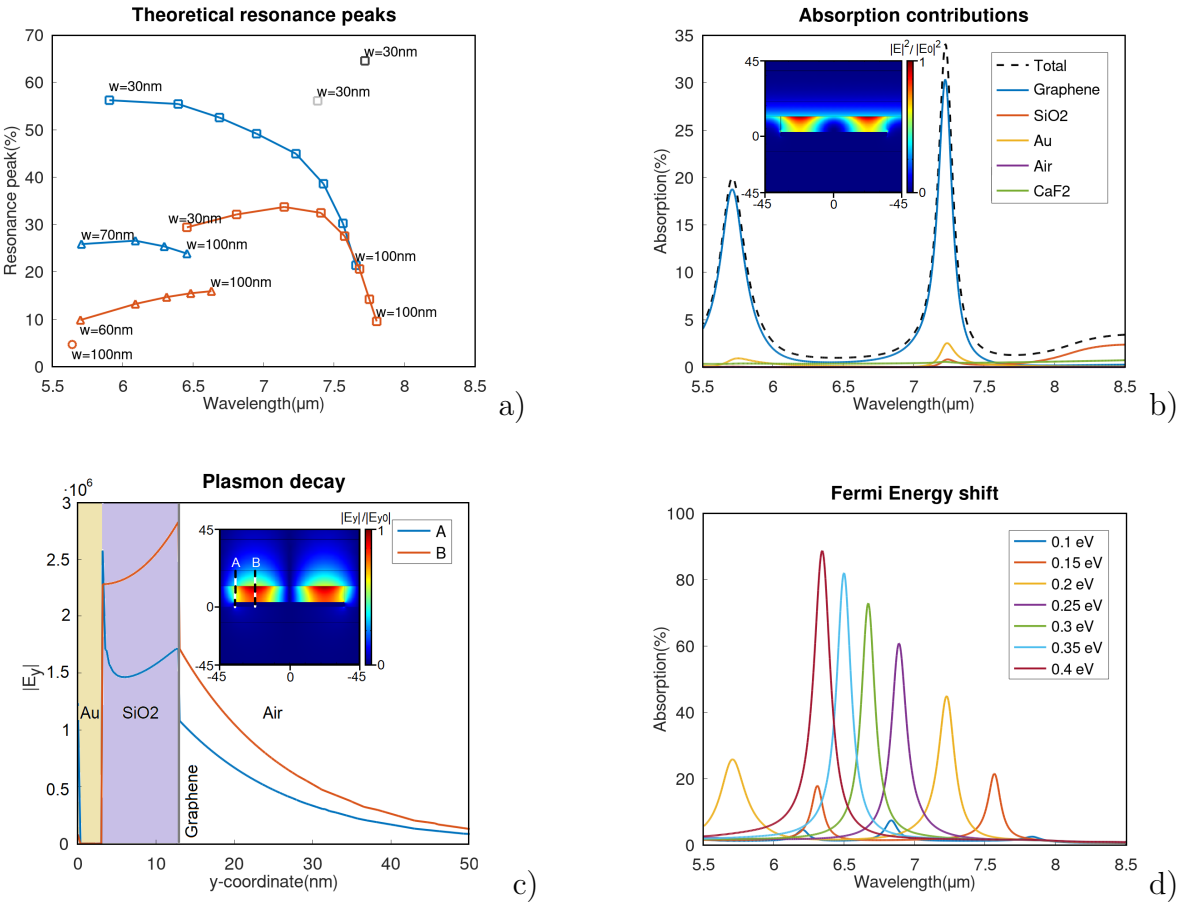

Figure 3: **a)** Resonance peaks for different ribbon widths and separations. Squares, triangles and circles represents 1^{st}, 2^{nd} and 3^{rd} AGPs modes, respectively. Blue and orange data represents a ribbon separation of $s = 20nm$ and $s = 40nm$, respectively. Light and dark grey data represents GPs modes in graphene nanoribbons with separations of $s = 20nm$ and $s = 40nm$, respectively. **b)** Absorption contributions for the different parts of the design for $w = 70nm$ and $s = 20nm$. The contributions are obtained with the power dissipation integral $(1/2)\int\int_S \omega Im(\varepsilon_r)\varepsilon_0|E|^2 dS$, [14], normalized with the incident power. **c)** Absolute value of the y-component of the AGPs field at two different points for the inset. **d)** Absorption curves for different Fermi Energies. Figures **a)** and **d)** are normalized with the absorption spectra of the system without graphene layer.

The second nano-surface consist on a 2D H-shaped nano-antenna slot of gold on a CaF_2 substrate covered with a graphene layer, fig. 4a, 4b. The objective of this design is to study the graphene-metal contact for the GPs generation, as studied in [16, 17]. The thickness of the gold layer is selected to 4 and $15nm$, and the size of the H-shaped nano-antenna is described by the lengths L_x and L_y, the periodicity Λ_x and Λ_y and the slot aperture w, see figure 4a. As commented in [17] for gold ribbons and slot ribbons, the GPs modes will be determined by the free metal space. In our case, due to the geometry of the system, the GPs modes are also dependent of the plasmonic and LC resonances of the metallic nano-antenna [9], which can be selected by changing the field polarization. For simplification, the ratios Λ_x/L_x and Λ_y/L_y are fixed to 1.2 and the length $L_x = 1\mu m$.

Figure 5a represents the first GPs mode resonance peaks for the field polarised along the y-axis (TM) for different values of w and L_y, for both gold thickness, and in backlight and normal angle incidence. It can be seen that the change in the slot aperture shift the GPs mode, as commented in [17]. Also, the increase in the arm length L_y contribute to reduce the resonance peak value of the GPs because for larger L_y values the bare H-shaped nano-antenna absorption baseline is also higher due his own plasmonic resonance, [9], hiding the GPs modes. Finally, it can also be seen that for thicker gold layers the resonance peaks are shifted towards smaller wavelengths and their values are reduced. The shift of the peaks is due to a change in the effective refractive index of the graphene surroundings, which changes the graphene plasmon dispersion, and the reduction of the peak values due the increase of the gold absorption due thicker layer.

In figure 5b it can be seen that the graphene slot is able to absorb and confine the incident electric field at the resonance frequency, but his contribution is not as high as the one seen in the previous nano-structure, fig. 3b. Moreover, the gold layer has also a big absorption contribution along all the range, which hides the graphene absorption, as commented above. By other hand, it must be taken into account that the graphene absorption is calculated along all the H-shaped slot, but in the inset it can be seen that the major part of the field is stored in the central arm, so all the absorption is high concentrated in that region. Figure 5b is done with $w = 90nm$, $L_y = 600nm$ and gold thickness of $4nm$.

Figure 5c shows the plasmon field decay along de z-axis for $y = w/4$ at the x-coordinates showed in the inset. The plot shows that the field is high enhanced in the H-shaped metal slot, but high fields are also obtained in the graphene vicinity. The decay is obtained as the absolute value of the z-component of the electric field, $|E_z|$.

Lastly, also for $w = 90nm$, $L_y = 600nm$ and gold thickness of $4nm$, the plasmon dispersion is plotted for different Fermi Energies, fig. 5d. The shift of the resonances against the change of Fermi Energy proves the generation of GPs.

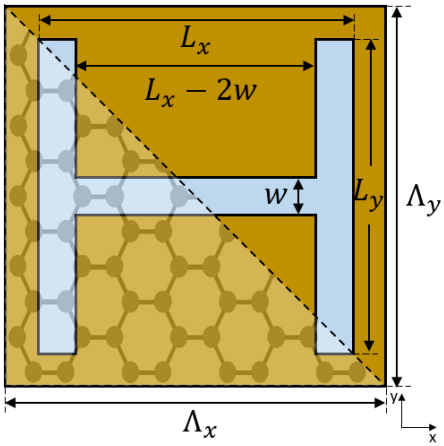

a)

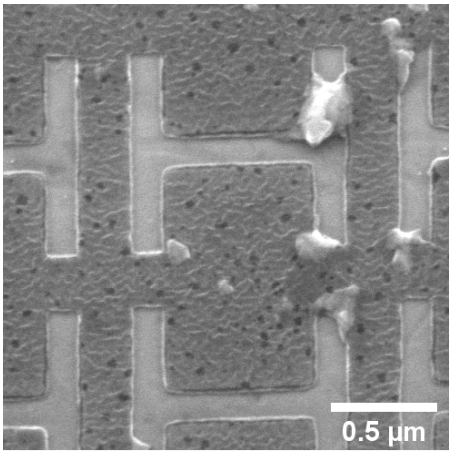

b)

Figure 4: **a)** Squematic representation of metal-graphene H-shaped sensor. **b)** SEM image of the sensor.

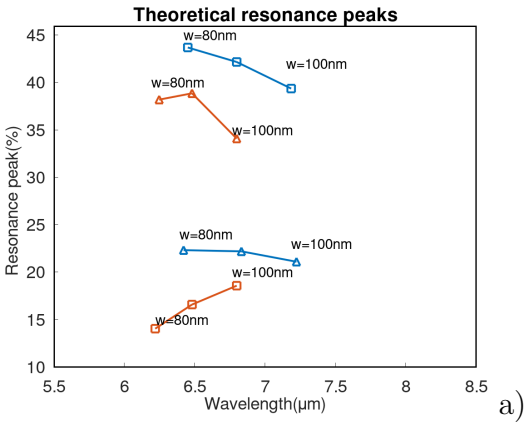

a)

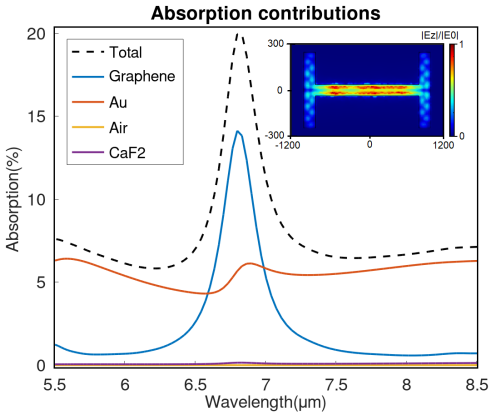

b)

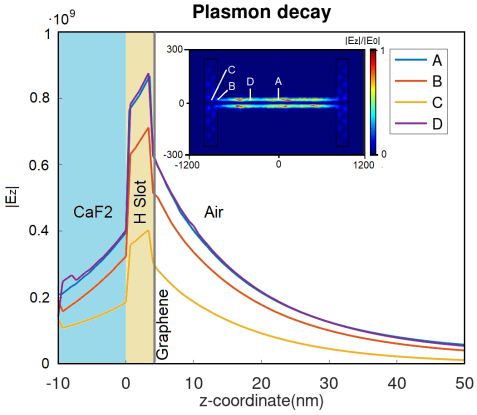

c)

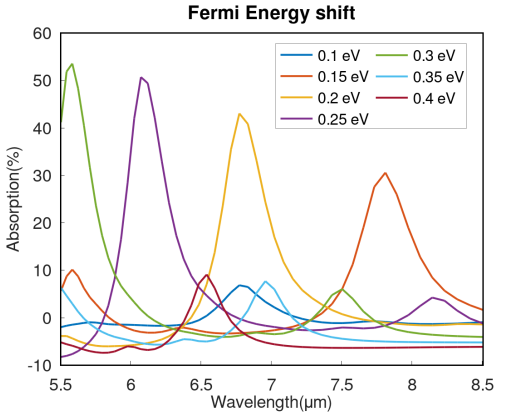

d)

Figure 5: **a)** Resonance peaks for different slot widths, L_y and gold layer thickness. Squares and triangles represents $L_y = 600nm$ and $L_y = 1200nm$, respectively. Blue and orange data represents a gold layer thickness of $4nm$ and $15nm$, respectively. **b)** Absorption contributions for the different parts of the design for $w = 90$, $L_y = 600nm$ and $4nm$ of gold. The contributions are obtained as in fig. 3b. **c)** $|E_z|$ decay in the $y = w/4$ plane. **d)** Absorption curves for different Fermi Energies. Figures **a)** and **d)** are normalized with the absorption spectra of the system without graphene layer.

5. Experimental measurements

To fabricate the nano-structured sensors, first a thin gold layer is grow over the CaF_2 following the method described in [8]. For the AGPs sensor, SiO_2 is evaporated over the gold layer. For the nano-ribbon and H-slot patterming, high-resolution $50kV$ e-beam lithography and subsequent reactive ion etching in an Ar plasma are used. To finish, wet transfer method using CVD grown graphene is done over the surfaces.

To characterize the nanostructures, measurements with a FTIR microscope were realized. FTIR technique allow to measure the reflection and transmission spectra of a sample, which are related with his absorption, by sending IR light, $(2-17)um$ in our case, in space region with sizes bigger than $20 \times 20\mu m$. For both nano-structured sensors, experimental measurements are normalized with the signal obtained on un-pattern surfaces. To compare experimental measurements with theoretical simulations, FEM simulations with measured geometrical parameters and more realistic graphene properties ($\tau_G = 30fs$ and $E_F = 0.1eV$) are done.

For the AGPs nano-structure, TM polarization, E_x, perpendicular to the nano-ribbons is used, so graphene plasmons can be excited as argued in [19]. Geometrical dimensions measured with SEM, fig. 2b, shows that $w = 55nm$ and $s = 25nm$.

Preliminary measurements of reflection, fig. 6a, and transmission, fig. 6b, show hints of resonant modes at $\lambda \approx 8\mu m$ and $\lambda \approx 6.5\mu m$. These resonances are at similar wavelengths to the ones obtained with FEM simulations for AGPs modes, except for small shifts in wavelength that can be due the contour of the fabricated nano-ribbons. However, the reflection and transmission baselines of experimental measurements and FEM simulations are different, which can be due the difference between experimental and simulated material dispersion models. In order to visualize correctly the resonances in both experimental and simulated results, figures 6a and 6b are normalized from the minimum to the maximum value of reflection and transmission, respectively. In fact, experimental reflection/transmission baseline is higher/lower than the one obtained in the simulations.

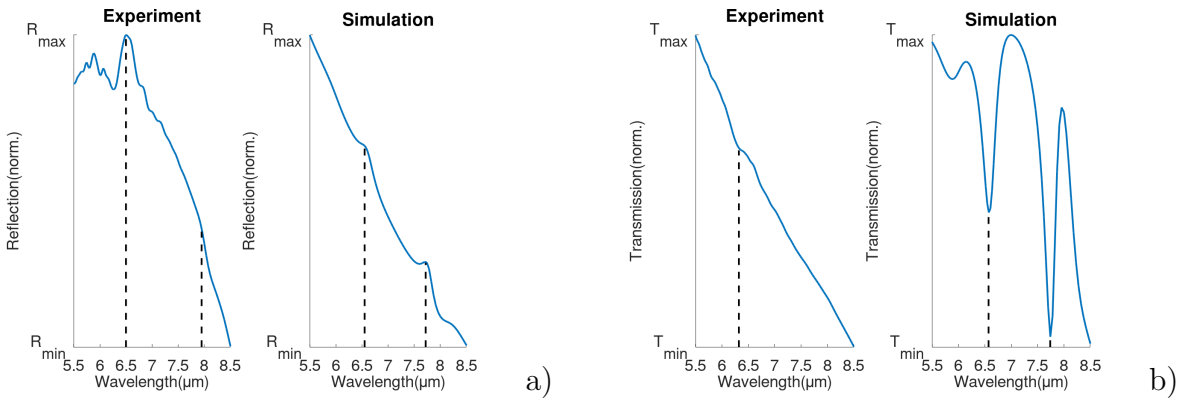

Figure 6: Experimental and simulated reflection, **a)**, and transmission, **b)** for the AGPs sensor with TM polarization.

For the hybrid graphene-metal H-shaped nano-antenna slot, TM polarization, E_y, is used in order to couple the plasmonic mode of the metallic H-shaped nano-antenna slot, [9], with the GPs mode of the central arm of the H-shape. The geometrical dimensions of the H-shaped slot measured with SEM, fig. 4b, shows that $L_x = 1000nm$, $L_y = 600nm$, $\Lambda_x/L_x = \Lambda_y/L_y = 1.2$ and $w = 90nm$.

In figures 7a and 7b experimental measurements and FEM simulations with the measured geometry are shown. First, notice that in the FEM simulations two small GPs modes appears in $\lambda \approx 7\mu m$ and $\lambda \approx 9.5\mu m$. For the experimental measurements, hints of these modes can be seen as resonances at the mentioned wavelengths, however they seems to be slightly shifted. The resonance at $\lambda \approx 7\mu m$ is more visible in the transmission signal than in reflection. It must be taken into account that the mentioned shift move the resonance towards the CO_2 absorption bands at $\lambda \approx 6\mu m$ hiding them. On the other hand, the resonance at $\lambda \approx 9.5\mu m$ can only be seen in reflection due broader experimental baseline curve. As for the previous design, the mentioned shifts may be due the contour modifications between the simulated and the fabricated geometry. As in the previous nano-structured sensor, the measured reflection signal is higher than the simulated, and the transmitted signal lower in the measurements than in simulations. As before, it can be due the difference between the experimental and the used dispersion model of CaF_2. Also, in this case the gold layer thickness is $4nm$ so the phenomenological factor used to correct the damping in Lorentz's model as in [8] may need to be readjusted. These preliminary results show that combining nano-structured thin metal layers in combination with graphene allow to engineer plasmonic resonances with reflection and transmission signal baselines that can be adjusted depending on the application.

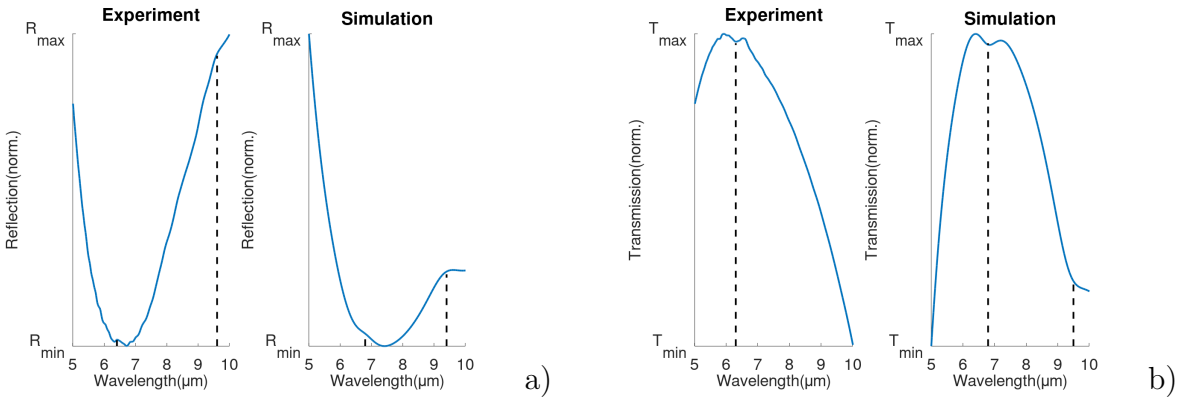

Figure 7: Experimental and simulated reflection, **a)**, and transmission, **b)** for the graphene-metal H-shaped nano-antenna slot sensor with TM polarization.

6. Conclusions

In this work, two nano-structured surfaces based on graphene and thin gold films have been investigated for plasmonic sensing applications in the mid infrared range. The structures have been designed by FEM simulations and show localized graphene

plasmon modes which are generated due the interaction between patterned thin metal layers and continuous graphene sheets. The designs allow to engineer graphene plasmon resonances at wavelengths difficult to engineer in patterned graphene and only require lithographic patterning of the metal layers, potentially leading to cleaner structures. Moreover the baseline of the reflected and transmitted signal can be changed by design. Preliminary experimental measurements on the two structures shows resonances that are in agreement with the simulations. Further experimental work must be done in order to study graphene plasmonic mode generation in these structures under electric gating.

Acknowledgments

I would like to give thanks to Dr. Valerio Pruneri for giving to me the opportunity of working with him and to Dr. Bruno Paulillo for his help and support during the realization of the master's thesis.

References

[1] . S. Schlücker *et al* . *Angew. Chem. Int. Ed.* **53**, 19, 4756-4795 (2014)
[2] . F. Neubrech *et al* . *Chem. Rev.* **117**, 7, 5110-5145 (2017)
[3] . J. Chalmers, P. Griffiths 2001 *In Handbook of Vibrational Spectroscopy* (Chichester: John Wiley Sons Ltd)
[4] . M. Fox 2010 *Optical Properties of Solids. 2nd Ed* (New York: Oxford University Press)
[5] . D. Rodrigo *et al* . *Science* **349**, 6244, 165-168 (2015)
[6] . Y. Li *et al* . *Nano Lett.* **14**, 3, 1573-1577 (2014)
[7] . K. K. Gopalan *et al* . *Nano Lett.* **18**, 9, 5913-5918 (2018)
[8] . R. A. Maniyara *et al* . *Nature Photonics.* **13**, 328-333 (2019)
[9] . B. Yuan *et al* . *Journal of Optics* **16**, 10 (2014)
[10] . D. Etezadi *et al* . *Light: Science & Applications* **6**, e17029 (2017)
[11] . R. Adato *et al* . *Nature Communications* **4**, 2154 (2013)
[12] . S. Kim *et al* . *Nano Lett.* **18**, 2, 971-979 (2018)
[13] . S. Chen *et al* . *ACS Photonics* **4**, 12, 3089-3097 (2017)
[14] . IH. Lee *et al* . *Nature Nanotechnology* **14**, 13, 313-319 (2019)
[15] . B. Vasic *et al* . *Appl. Phys. Lett.* **103**, 261111 (2013)
[16] . Y. Zhu *et al* . *Light: Science & Applications* **7**, 67 (2018)
[17] . Z. Li *et al* . *Appl. Phys. Lett.* **102**, 131108 (2013)
[18] . L. A. Falkovsky *et al* . *J. Phys.: Conf. Ser.* **129**, 012004 (2008)
[19] . H. Yan *et al* . *Nature Photonics* **7**, 394-399 (2013)
[20] . F. H. L. Koppens *et al* . *Nano Lett.* **11**, 8 (2011)
[21] . W. Gao *et al* . *ACS Nano* **6**, 9, 7806-7813 (2012)
[22] . R. L. Olmon *et al* . *Phys. Rev. B* **86**, 235147 (2012)
[23] . R. Kitamura *et al* . *Applied Optics* **46**, 33 (2007)
[24] . I. H. Malitson *et al* . *Applied Optics* **2**, 11 (1963)